Structure-guided mutagenesis of OSCAs reveals differential activation to mechanical stimuli

Sebastian Jojoa-Cruz[1], Adrienne E. Dubin[2], Wen-Hsin Lee[1], Andrew Ward[1]†

Affiliations

[1] Department of Integrative Structural and Computational Biology, Scripps Research, La Jolla, California 92037, USA.

[2] Department of Neuroscience, Scripps Research, La Jolla, California 92037, USA.

†Corresponding author

Correspondence to: A.B.W.: andrew@scripps.edu

Abstract (150-200 words)

The dimeric two-pore OSCA/TMEM63 family has recently been identified as mechanically activated ion channels. Previously, based on the unique features of the structure of OSCA1.2, we postulated the potential involvement of several structural elements in sensing membrane tension[1]. Interestingly, while OSCA1, 2, and 3 clades are activated by membrane stretch in cell-attached patches (i.e., they are stretch-activated channels), they differ in their ability to transduce membrane deformation induced by a blunt probe (poking). In an effort to understand the domains contributing to mechanical signal transduction, we used cryo-electron microscopy to solve the structure of *Arabidopsis thaliana* (At) OSCA3.1, which, unlike AtOSCA1.2, only produced stretch- but not poke-activated currents in our initial characterization[2]. Mutagenesis and electrophysiological assessment of conserved and divergent putative mechanosensitive features of OSCA1.2 reveal a selective disruption of the macroscopic currents elicited by poking without considerable effects on stretch-activated currents (SAC). Our results support the involvement of the amphipathic helix and lipid-interacting residues in the membrane fenestration in the response to poking. Our findings position these two structural elements as potential sources of functional diversity within the family.

30 **Introduction**

31 Mechanotransduction allows organisms to gather information about their external surroundings
32 as well as internal processes. Mechanically-activated (MA) ion channels are capable of sensing
33 mechanical stimuli and transducing this information to the cell as electrochemical signals[3]. MA
34 ion channels are diverse and capable of responding to different stimuli such as osmotic stress,
35 membrane deformation, touch, and hearing[3,4].

36

37 In our previous work, we identified OSCA/TMEM63 as a conserved family of MA ion channels
38 spanning several eukaryotic clades and having considerable diversity in the plant kingdom, where
39 species commonly have more than one paralog. For example, *Arabidopsis thaliana* has 15
40 members[2] and *Oryza sativa* L. *japonica* (rice), 11[5]. We demonstrated these channels can respond
41 to membrane stretch even more robustly than hypertonicity, originally thought to be the relevant
42 stimulus, with some members (OSCA1.1 and OSCA1.2) also able to respond to poke[2]. We used
43 cryo-electron microscopy (cryo-EM) to solve the structure of OSCA1.2 in a closed state in both
44 detergent (LMNG) and nanodiscs at high-resolution, identifying a new architecture for MA ion
45 channels that is structurally homologous to TMEM16 proteins[1]. Results from other groups are
46 consistent with ours[6-8]. Similar to the TMEM16 family, OSCAs are dimeric and each subunit has a
47 pore lined by transmembrane helices (TMs) 3 to 7, instead of a single pore along the symmetry
48 axes[1,6-8]. A hydrophobic gate on the extracellular half of the pore blocks ion flow. Additionally,
49 molecular dynamics (MD) simulations support our placement of the pore and position lipids along
50 an opening of the pore pathway in the transmembrane domain (TMD)[1].

51

52 Based on the unique structural characteristics of OSCA1.2, we proposed that two features might
53 be involved in sensing membrane deformation: the amphipathic helix (AH) located in the first
54 intracellular loop, and the Beam-Like Domain (BLD), composed of the two cytoplasmic
55 membrane-parallel helices and a hydrophobic hook that connects them and re-inserts itself into
56 the membrane[1]. Due to the close association of these two elements to the membrane, we
57 reasoned that they could serve as sensors of mechanical stimuli and transmit the signal to the
58 pore through interactions with the TMD. Additionally, a fenestration allows the membrane

access to the pore, and MD simulations placed lipids in close association with four positively charged residues in this area suggesting a potential role in gating[1]. We sought to determine whether these regions contributed to mechanotransduction.

Here, we used cryo-EM to determine a high-resolution structure of AtOSCA3.1, the first reported OSCA gene[9], in nanodiscs. In our initial characterization, OSCA3.1 responded to stretch but not poke[2]. Comparison of the OSCA3.1 structure reported here to previous structures of OSCA1.1[6] and OSCA1.2[1] revealed subtle differences. Structure-function analyses revealed the involvement of the AH and the lipid-interacting residues in the pore pathway of OSCA1.2 in the ability of the channel to respond to membrane deformation by poking. Our results suggest that these features are not only important for mechanotransduction or activation of OSCA1.2 by poking in OSCAs but may serve to tune the response of OSCA/TMEM63 members to diverse stimuli.

Results

Overall architecture of OSCA3.1 is similar to OSCA1.1 and OSCA1.2

We recombinantly tagged OSCA3.1 with EGFP at its C-terminus, expressed the construct in HEK293F cells, and purified it using Lauryl Maltose Neopentyl Glycol (LMNG) supplemented with cholesteryl hemisuccinate (CHS). The EGFP was removed by PreScission Protease cleavage, leaving a stretch of ten residues on the C-terminus. Purified protein was then reconstituted into nanodiscs and subjected to cryo-EM analysis, resulting in a 2.6 Å resolution symmetric reconstruction (Fig. 1a, Supplementary Fig. 1) sufficient to build a model of the majority of the protein (537 out of 724 residues) (Fig. 1b-c, Supplementary Fig. 2, Supplementary Table 1). Due to increased flexibility of the BLD relative to previous OSCA structures, we were unable to assign residue identity, and instead modeled it as two poly-Ala helices.

Overall, there is good agreement between OSCA3.1, OSCA1.1 and OSCA1.2 protomers[1,6] (Cα RMSD OSCA3.1-OSCA1.1: 1.243Å, OSCA3.1-OSCA1.2: 1.152Å, Fig. 1c). The pore profile of these OSCAs is maintained and the small radii towards the extracellular side suggests these channels

88 are in a closed/non-conductive state, as suggested by previous MD simulations[1,6] (Fig. 1d).
89 Likewise, the two π-helical turns in TM5 and TM6a seen in previous structures near the neck of
90 the pore are present at similar positions in OSCA3.1[1,8]. We identified multiple lipid-like densities
91 in one of our postprocessed maps (Fig. 1e, Supplementary Fig. 3). Notably, one of these densities
92 is located at the pore fenestration, at a position similar to that observed in previous MD
93 simulations of OSCA1.2[1], supporting the proposed occupation of the pore pathway by lipids.
94 Recent cryo-EM structures of AtOSCA1.2[10], and AtOSCA1.1 and human TMEM63A[11] also place a
95 lipid at a similar position.
96
97 Previously, the structure of OSCA3.1 was solved in a digitonin micelle[6], and more recently, in
98 LMNG[11]. The similarity of our nanodisc sample to these detergent structures suggests that the
99 use of detergent did not affect the conformation or oligomerization of OSCA3.1, similar to
100 previous results with OSCA1.2[1,7] (Supplementary Fig. 4a-b). However, the inter-subunit cleft in
101 the nanodisc structure is wider due to outward movements of innermost TMs ranging from ~4-
102 8Å (Supplementary Fig. 4c) relative to the digitonin sample, which was recently denoted as an
103 "extended" state[11]. Thus, our nanodisc structure represents a further "extended" state than the
104 one found both in digitonin and LMNG micelles[11] (Supplementary Fig. 4d). Whether these
105 differences represent biologically meaningful states, an effect of the lipid environment
106 (detergent vs lipids), or inherent flexibility of the channel remains to be determined. Additionally,
107 our structure enabled a higher degree of certainty in the residue assignment relative to the initial
108 digitonin structure, particularly for TM0 where sidechains were not previously modelled[6].
109 Consequently, we have shifted the registry of TM0 by two residues relative to the detergent
110 structure, in agreement with the LMNG structures[11].
111
112 **Mutation of key residues in the amphipathic helix abrogates poke but not stretch responses in**
113 **OSCA1.2**
114 Structures of AtOSCA1.1, rice and At OSCA1.2, and OSCA3.1 (Fig. 2a, Supplementary Fig. 5), as
115 well as sequence alignment, suggest that the AH between TM0 and TM1 of OSCAs is a conserved
116 feature of these channels. AHs can serve as both membrane anchors and sensors of membrane

117 deformation[12], and they are present in many MA ion channels[1,13-15]. There is evidence for their
118 involvement in mechanical force transduction; for example, in the bacterial mechanosensitive
119 channel of large conductance MscL, an AH in the cytoplasmic side of the bilayer links membrane
120 tension to protein conformation (Supplementary Fig. 6a,b)[14]. Interestingly, structures of
121 members of the TMEM16 family, structural homologs of OSCAs, have a similarly placed helix in
122 this region; however, it is located in the cytosol and does not present amphipathic properties
123 (Supplementary Fig. 6c-e)[16-18]. Involvement of TMEM16A in the detection of mechanical forces
124 in myocytes and bile ducts was dependent on calcium influx (potentially caused by an upstream
125 MA cation channel) and not a direct response to the mechanical stimulus[19,20]. To our knowledge,
126 characterization of TMEM16 proteins as MA ion channels has not been reported. Based on these
127 observations, we mutated the membrane-facing residues at each end of the AH of OSCA1.2 in an
128 effort to decrease its propensity to interact with the membrane. Single (W75K or L80E) and
129 double (W75K/L80E) mutants in OSCA1.2 strongly abrogated the response to indentation of the
130 membrane with a blunt glass probe (poke) (WT: 47 of 51 cells produced MA currents; W75K: 3 of
131 24; L80E: 2 of 16; W75K/L80E: 2 of 24; Fig. 2b, top panel). Moreover, in OSCA1.2$_{W75K/L80E}$, a larger
132 displacement of the membrane by the probe relative to the WT appeared to be needed to
133 observe currents ("apparent threshold"; WT: 5.3 ± 0.5 µm (N = 46; mean ± S.E.M.), W75K/L80E:
134 15.3 ± 2.3 µm (N = 2), with the none-responsive W75K/L80E cells rupturing at a 13.0 ± 0.5 µm (N
135 = 22); Fig. 2b, bottom panel). The insensitivity to the poking stimulus was not due to poor
136 membrane trafficking of these constructs (see below). The loss of sensitivity of cells expressing
137 these mutant constructs to poking suggests that the AH of OSCA1.2 plays an important role in
138 this mechanically-activated response.
139
140 We then tested whether these mutations in the AH affected the response of OSCA1.2 to stretch.
141 Contrary to what was observed during poking, all cell-attached patches revealed stretch-
142 activated currents (WT: 25 of 26 cells; W75K: 3 of 3; L80E: 5 of 5; W75K/L80E: 11 of 11; Fig. 2c,
143 top panel; electrode resistances were similar in all cases (see Figure legend)). Despite differences
144 in the amplitude of macroscopic currents, which could be explained by variation in expression
145 levels, all mutant channels were activated at similar thresholds (WT: -48 ± 5 mmHg (N = 25);

146 W75K: -56 ± 11 mmHg (N = 3), L80E: -41 ± 6 mmHg (N = 5), W75K/L80E: -53 ± 8 mmHg (N = 11))
147 (Fig. 2c, bottom panel). In all cases, there was variability in the rate of inactivation from
148 moderately fast to extremely slow (data not shown). Overall, the observed stretch response of
149 OSCA1.2 was apparently not affected by the mutations we introduced.
150
151 Subsequently, we mutated the proline in the OSCA1.2 AH to the corresponding arginine in
152 OSCA3.1 to determine whether this difference impacts the ability of OSCA3.1 to robustly
153 transduce the poke stimulus; this change ($OSCA1.2_{P77R}$) had no effect on the poke response
154 (Supplementary Fig. 7).
155
156 It is worth noting that in our initial characterization, OSCA3.1-expressing cells produced SAC while
157 poke did not induce observable currents[2]. However, in the present experiments we were able to
158 record poke-activated currents mediated by OSCA3.1 on a few occasions ($OSCA1.2_{WT}$: 6 of 6 cells;
159 $OSCA3.1_{WT}$: 3 of 10) (Supplementary Fig. 8a). The apparent threshold for OSCA3.1 activation by
160 poke-induced membrane displacement tended to be higher than for OSCA1.2 but the difference
161 was not statistically significant ($OSCA1.2_{WT}$: 10.4 ± 1.2 µm (N = 6; mean ± S.E.M.); $OSCA3.1_{WT}$:
162 13.8 ± 0.9 µm (N = 3)) (Supplementary Fig. 8b), perhaps due to the low numbers of responsive
163 cells analyzed. These data suggest that the poking stimulus is capable of activating OSCA3.1 but
164 the stimulus intensity required is close to the rupture point of the HEK293T-Piezo1-knockout
165 (HEK-P1KO) cells used in our assay.
166
167 **Replacing the OSCA3.1 Beam-Like Domain (BLD) in OSCA1.2 had no effect on stretch-induced**
168 **currents but decreased the apparent sensitivity of the cells to poke**
169 One of the unique features of OSCAs is the presence of the BLD, a hydrophobic hook that, by
170 inserting itself into the membrane, may serve as an anchor that could potentially be displaced
171 under tension[1,7,8]. Hydrogen/deuterium exchange mass spectrometry (HDXMS) of rice OSCA1.2
172 indicated that the helix of the BLD closest to the membrane undergoes less deuterium exchange
173 and potentially remains associated to a neighboring surface[8], hinting at an important interaction
174 with TM6b. In OSCA3.1, the BLD is poorly resolved, likely due to flexibility (Fig. 1c). To test

175 whether the increased flexibility in this region affects MA responses, we replaced the BLD of
176 OSCA1.2 with the BLD of OSCA3.1 (Fig. 3a). HEK-P1KO cells expressing the chimera $OSCA1.2_{OSCA3.1-}$
177 $_{BLD}$ produced similar MA currents in both poke and stretch assays (Fig. 3b,c) with the exception
178 that a slightly stronger displacement stimulus was required to activate the mutant channels (Fig.
179 3b, bottom panel). These data suggest that the BLD is not responsible on its own for the ability
180 of the channels to be activated by poking, however, it appears to play a role. As expected for
181 similar SAC from cells expressing OSCA1.2 and OSCA3.1, there was no obvious change in SAC
182 when the OSCA1.2 BLD was replaced with the OSCA3.1 BLD. It should be noted that the BLD
183 tolerates a certain degree of mutation as sequence alignment in this region shows higher
184 variability than other secondary structures of OSCAs (Supplementary Fig. 5). Thus, we cannot rule
185 out that in the OSCA1.2 background, the BLD of either channel is capable of performing a similar
186 role.
187
188 **Substitution of potential lipid-interacting lysine residues for isoleucine abrogates the poke**
189 **response in OSCA1.2**
190 Lipids play an important role in the stability and function of ion channels[21]. In TRAAK, a eukaryotic
191 mechanosensitive channel, occlusion of the pore by a lipid acyl chain has been proposed as a
192 gating mechanism[13,22]. In the volume-regulated channel SWELL1 lipids block the pore in the
193 closed state[23]. In the bacterial mechanosensitive channel MscS, the occupation of lipid pockets
194 may determine channel conformation[24,25], and in FLYC1, a Venus flytrap homolog of MscS,
195 conformational changes may allow lipids to access the pore and occlude ion conduction[26].
196 Moreover, exposure of inside-out patches from OSCA1.1-expressing HEK cells to lyso-
197 phosphatyidylcholine (LPC) enhanced channel response to stretch[6].
198
199 Previously, we identified four lysine residues in OSCA1.2 located in TM4 and TM6b at the pore
200 fenestration. These residues interacted with lipid phosphate head groups throughout the
201 duration of our MD simulations[1]. The OSCA3.1 structure revealed that two of these lysine
202 residues (K435 and K536 of OSCA1.2) have been replaced by isoleucine (I423 and I525,
203 respectively), which are expected to reduce the interaction with lipid phosphate head groups

204 (Fig. 4a). To test for the contribution of these lipid-interacting residues to channel
205 mechanosensitivity, we measured poke- and stretch-induced currents in the double mutant
206 OSCA1.2$_{K435I/K536I}$ (Fig. 4b,c). The double mutant responded poorly to poking, with only 1 out of
207 20 cells producing currents upon mechanical stimulation (K435I/K536I: -365 pA (N = 1)) (Fig. 4b,
208 comparison made to WT data acquired on the same days). This finding was not due to poor
209 expression of the double mutant in HEK-P1KO cells; the SAC I_{max} observed in cell-attached patches
210 was similar to WT (Fig. 4c, top panel). Furthermore, the mutant could be activated by stretch at
211 similar thresholds to WT (WT: -43 ± 10 mmHg (N = 6); K435I/K536I: -60 ± 10 mmHg (N = 7)) (Fig.
212 4c, bottom panel), and similar stretch-response dependence (i.e., similar pressures required to
213 elicit half-maximal currents (P_{50}) and slope) (Fig. 4d). Although macrocurrent amplitudes in SAC
214 recordings tended to be lower than WT tested on the same day, the ~2-fold difference unlikely
215 accounts for the ~20-fold fewer responsive cells (Fig. 4b,c). Taken together, these results suggest
216 that loss of positively charged sidechains in the fenestration selectively impairs poke-induced
217 responses of OSCA1.2 under physiological conditions, but not its responsiveness to the stretch
218 stimulus.
219
220 **Discussion**
221 Here we performed structure-function studies to determine the molecular underpinnings of
222 mechanical activation of OSCA ion channels. We solved the structure of OSCA3.1 at a resolution
223 of 2.6 Å in a non-conductive state and revealed a marked structural conservation to previous
224 OSCA orthologs. The final map presented several lipid-like densities surrounding the channel,
225 including one density close to the pore and several densities populating the inter-subunit cleft.
226 This ion channel was reported to be activated by stretch in cell-attached patches but insensitive
227 to a poke stimulus using a blunt glass probe[2]. Comparisons between the structures of OSCA1.2,
228 which is robustly activated by both poke and stretch, to OSCA3.1, which is only robustly
229 activated by stretch, suggested 3 domains that might contribute to gating during a poke
230 stimulus. First, a conserved short amphipathic helix (AH) which sits at the membrane interface
231 reminiscent of a similar feature in other MA ion channels like MscL[14], Piezo1[15], MscS[27], and
232 TRAAK[28]. Second, side chains in TM4 and TM6b in the vicinity of the membrane fenestration

233 may have differential interactions with lipids as indicated by MD simulations of OSCA1.2. Third,
234 the beam-like domain (BLD) that contains 2 helices and linker that hooks around the
235 cytoplasmic surface into the membrane in OSCA1.2 but is less well-resolved in the OSCA3.1
236 map presumably because it is not intimately associated with the channel/membrane.
237 Mutagenesis of the AH and residues at the fenestration in OSCA1.2 largely abrogated its
238 response to poking without affecting its activation by stretch; replacing the BLD with that from
239 OSCA3.1 only slightly impaired the response to poking, having no effect on stretch-induced
240 activation.
241
242 Residues in the AH were mutated to either confer more of an OSCA3.1 character or tend to
243 make the domain less likely to interact with the membrane, similar to the TMEM16 family that
244 are not thought to be directly activated by mechanical stimuli. Swapping the divergent residue
245 in the AH of OSCA1.2 with its equivalent in OSCA3.1 (OSCA1.2$_{P77R}$), had no negative impact on
246 the sensitivity to poking. These data suggest that the difference in poke sensitivity between
247 OSCA1.2 and OSCA3.1 is not due to the AH itself. However, when mutations were incorporated
248 to presumably destabilize the interaction of the AH domain with the membrane
249 (OSCA1.2$_{W75K/L80E}$), fewer cells could be activated by poking to similar stimulus strengths while
250 stretch-activation of channels was not impaired. Although a WT OSCA1.2 AH is critical for
251 normal poke-induced channel opening, these mutations do not hinder gating by membrane
252 stretch.
253
254 Substituting the BLD of OSCA1.2 for that of OSCA3.1 had little effect on poke- or stretch-
255 activated responses. Although these results suggest that the BLD may not be involved in
256 modulating the MA response of OSCA1.2, a recent report suggested evolutionary coupling of 3
257 sets of residues in the BLD and TM6b that may form electrostatic interactions between these
258 domains[10]. The evolutionarily favored residue identities at these sites constitute three potential
259 salt bridges: **R/K**257-**E**557, **E**260-**R**553, and **R/K**261-**E/D**554 (based on OSCA1.2 numbering).
260 These sites in OSCA1.2$_{OSCA3.1\text{-}BLD}$ chimera correspond to N257**K**-**E**557, D260**A**-**K**553, and Y261**R**-
261 **D**554 (mutation-interacting residue), perhaps leaving intact 2 out of 3 potential salt bridges and

262 maintaining its influence (Supplementary Fig. 5). It is worth noting that a similar chimera of
263 AtOSCA1.2 with the IL2 domain of the human ortholog TMEM63A (OSCA1.2$_{63A\ IL2}$), containing
264 most of the intracellular domain which includes the BLD as well as the dimerization domain,
265 presented little inactivation of SAC akin to monomeric TMEM63A$_{WT}$[29]. This behavior was not
266 due to an inability of OSCA1.2$_{63A\ IL2}$ to dimerize, as the monomeric OSCA1.2$_{5Mu}$, obtained by
267 disrupting the dimer interface with 5 mutations while maintaining OSCA1.2$_{WT}$ BLD, exhibited
268 pressure-induced SAC gating similar to OSCA1.2$_{WT}$[29]. This new evidence, taken together with
269 the decrease in the apparent poking sensitivity of the OSCA1.2$_{OSCA3.1\text{-}BLD}$ chimera in this study,
270 suggests that the BLD plays a role in the force-induced gating of the OSCA family.
271
272 The structure of OSCA3.1 exhibits an open fenestration similar to OSCA1.2 and lipids are expected
273 to populate this area[1], similar to lipid occlusion of the pore in other MA ion channels such as
274 TRAAK[13] and MscS[24,25]. Our results suggest that TM4 and TM6b interactions with lipids may
275 contribute to activation during poking. Modification of OSCA1.2 residues to match those of
276 OSCA3.1 (OSCA1.2$_{K435I/K536I}$) produced an OSCA3.1-like phenotype (MA currents are observed in
277 response to stretch but rarely to poke). These mutant channels are not completely insensitive to
278 poking but appear to have a very high threshold to activate, one that is often beyond the point
279 of cell rupture by the stimulus (similar to that seen with OSCA1.2$_{W75K/L80E}$). Notably, TM4 in
280 TMEM16 lipid scramblases and TM6 in both TMEM16 scramblases and channels undergo
281 conformational changes during activation[16,17,30]. The loss of positive charges in OSCA3.1 may
282 weaken the interactions between residues and lipids, similar to MscS where charge
283 neutralization of the lipid facing residue R59 by the introduction of a leucine strongly altered
284 gating, potentially by disturbing a salt bridge with a lipid phosphate[31,32]. A weaker interaction
285 could decrease the tension generated by the lipids upon mechanical stimulus, hence increasing
286 the force needed to open the channel, as seen in our poke experiments. A similar argument could
287 be made for the AH of OSCAs: by disturbing its coupling with the lipid bilayer, a greater stimulus
288 might be needed to activate the channel. It is also important to note that the membrane of a
289 plant cell contains a different lipid composition than that of HEK293 cells used in our assays, and

290 thus these lipids, or association with the plant cell wall, may alter how these channels respond
291 to physiological stimuli in vivo.
292
293 The phenotypes of OSCA1.2$_{W75K/L80E}$ and OSCA1.2$_{K435I/K536I}$ suggest a mechanism recruited by
294 poking is no longer able to adequately activate OSCA1.2$_{W75K/L80E}$ and OSCA1.2$_{K435I/K536I}$ channels.
295 Since the factors contributing to channel activation in the poking assay are not understood, we
296 can only speculate as to mechanisms underlying the loss of sensitivity to poking in these mutants.
297 Our results suggest that these stimuli are sensed by different features of OSCA channels, akin to
298 the well-studied ThermoTRP channels[33-35]. Polymodal activation mechanisms have been recently
299 reported for the MA channel PIEZO2 where a mutagenesis approach revealed differential effects
300 on the ability to respond to poking and stretch[36]. Nonetheless, the discrepancy could be due to
301 inherent methodological differences between these two assays, as whole-cell recordings during
302 poking involve channels in inaccessible membranes (at the cell-substrate interface) and channel
303 interactions with extracellular and intracellular components[37], while the stretch assay is limited
304 to recording channels inside the patch.
305
306 Overall, the analysis of these mutants demonstrates the involvement of the AH and residues at
307 the membrane fenestration in the MA response of OSCAs, as we initially proposed[1]. The
308 participation of residues from TM4 and TM6 hint at further similarities with TMEM16 family, but
309 to what extent is unknown. Perhaps the most surprising result is the selective disruption of poke-
310 activated currents of OSCA1.2 without affecting its response to membrane stretch, which
311 suggests that changes in these features could serve to fine-tune the response to certain
312 mechanical stimuli and may be a source of functional diversity within this large family. The
313 structures and characterizations presented here and in our previous work[1,2] will prove
314 fundamental in assessing the physiological consequences of these differences and further
315 understanding the role of the OSCA/TMEM63 family.
316
317
318

319 **Materials and methods:**

320 Expression constructs

321 For structural studies, the OSCA3.1 (UniProt ID: Q9C8G5) coding sequence was synthesized using
322 optimized codons for expression in human cells and subsequently cloned into the pcDNA3.1
323 vector used in our previous report[1]. In this plasmid, the C terminus of the protein sequence is
324 followed by a PreScission Protease cleavage site, EGFP and a FLAG tag.

325

326

327 Protein expression and purification

328 Samples of OSCA3.1 in nanodisc were obtained following the same method reported previously
329 for OSCA1.2 in nanodiscs[1], with the exception of the detergent used. Instead of beta-D-
330 maltopyranoside (DDM), we used Lauryl Maltose Neopentyl Glycol (LMNG) due to increased
331 yields. Thus, the detergent composition of the solubilization and wash buffers was 1%/0.1% and
332 0.01%/0.001% LMNG/cholesteryl hemisuccinate (CHS), respectively. Fractions from Size
333 Exclusion Chromatography (SEC) corresponding to the OSCA3.1 in nanodiscs peak were
334 concentrated to 3.2mg/mL (corrected using the extinction coefficient of OSCA3.1).

335

336

337 Cryo-EM sample preparation and data collection

338 3.5 µL of OSCA3.1 at 3.2mg/mL were frozen using the same conditions as OSCA1.2 samples[1].
339 Grids were imaged on a Titan Krios (ThermoFisher) operating at 300 kV with a K2 Summit direct
340 electron detector (Gatan), with pixel size of 1.03Å (nominal magnification of 29,000x). A total of
341 38 frames were collected per movie, adding to a total dose of ~50 electrons per $Å^2$. Automated
342 image collection was done through Leginon[38] using a defocus range of -0.4 to -1.5 µm. A total of
343 8,375 movies were collected.

344

345

346 Cryo-EM image processing

347 During collection, movies were aligned and dose-weighted using MotionCor2[39]. The resulting
348 micrographs were imported into cryoSPARCv2.5[40] and CTF values were estimated through Gctf[41].
349 ~300 particles were manually picked from ~10 micrographs and subjected to 2D classification to
350 obtain templates. Template picking was tested on 20 micrographs and particles used to generate
351 better 2D templates. These templates were later used to pick particles on ~1600 micrographs.
352 The resulting ~900k particles were subjected to, in order, 2D classification, *ab initio*
353 reconstruction, 2 rounds of heterogeneous refinement, homogeneous refinement and non-
354 uniform refinement to obtain an initial 3D reference, which reached high-resolution. Unless
355 otherwise specified, C2 symmetry was applied to all homogeneous, non-uniform and RELION 3D
356 refinements.
357
358 For the full dataset, 8,375 movies were imported into cryoSPARCv2 and subjected to full-frame
359 motion correction followed by Gctf estimation. Given the large size of the dataset, and the fact
360 that initial processing had returned a high-resolution structure, we decided to apply a 2.6 Å CTF
361 cutoff to reduce the number of micrographs to 3,068 and speed up processing. Templates were
362 generated based on the initial 3D reference. Template picking, followed by local motion
363 correction and 2D classification resulted in 1,913,316 selected particles for our initial stack. *Ab*
364 *initio* reconstruction produced 3 classes, and heterogeneous refinement was performed on the
365 two worst classes. The resulting best class was combined with the best class from *ab initio* and
366 used for two rounds of heterogeneous and homogeneous refinements. The heterogeneous
367 refinement of the first round was done without symmetry, from that point onwards, C2
368 symmetry was imposed unless otherwise specified. Only particles belonging to the best class
369 were selected for further processing (318,249). Non-uniform refinement, followed by 2 rounds
370 of local refinement (without imposing symmetry), were performed on these particles before
371 exporting them into RELION-3.1[42,43]. The particle stack underwent the following process in
372 RELION. 3D refinement, CTF refinement, 3D refinement with global angular searches, 3D
373 refinement using SIDESPLITTER (SS)[44], and two rounds of CTF and 3D refinements using SS. Unless
374 specified, all 3D refinements were limited to local angular searches. 3D classification without
375 alignment (no imposed symmetry) was performed on the particle stack and the best class,

376 comprising 197,944 particles, was subjected to a final 3D refinement with SS. The map was
377 sharpened separately with LocalDeblur[45] through Scipion[46-48] and DeepEMhancer using the
378 'highRes' model[49]. The FSC and local resolution of the map was calculated through RELION.
379
380
381 Model building and refinement
382 A homology model for OSCA3.1 was obtained through SWISS-MODEL[50], using as template the
383 structure of OSCA1.2 in nanodiscs (PDB: 6MGV)[1]. Iterative rounds of building in Coot[51,52] and real
384 space refinement in Phenix[53,54] and Rosetta[55] were used to generate the final model. SMILES
385 codes for the ligands were used to obtain the appropriate restrains using eLBOW[56]. Model
386 validation was carried out with MolProbity[57] and EMringer[58] to the LocalDeblur map. Phenix
387 mtriage[59] was used to calculate the map to model FSC. The final model comprises residues 2-102,
388 154-231, 307-388, 410-476, and 489-697, for a total of 537 out of 724 residues in OSCA3.1
389 sequence. A segment of the BLD was modelled as poly-A helices and registry was tentatively
390 assigned based on sequence and structure alignment to OSCA1.2[1]: residues 234-246 and 280-
391 303 assigned as IL2H2 and IL2H3, respectively. Pore profiles were predicted by CHAP[60,61].
392 Structure figures were made with PyMOL[62], UCSF Chimera[63] or UCSF ChimeraX[64]. Amino acid
393 sequence alignment was obtained from Clustal omega[65] and represented with ESPript3[66].
394 Sequences used for the alignment were the same as previous publication[1], but the display was
395 limited to the *Arabidopsis thaliana* OSCAs with solved structure.
396
397
398 Generation of mutants, cell culture and transfections
399 A vector containing OSCA1.2 pIRES2-mCherry was used for electrophysiology experiments[2]. The
400 W75K substitution was introduced using Q5 site-directed mutagenesis kit (New England Biolabs,
401 NEB). Substitutions L80E, K435I, and K536I were introduced using QuikChange multi site-directed
402 mutagenesis kit (Agilent). For the BLD chimera, OSCA1.2 pIRES2-mCherry vector and the BLD of
403 OSCA3.1 were separately amplified by PCR using Q5 High-Fidelity 2X Master Mix (NEB), followed

404 by fragment assembly using Gibson Assembly Master Mix (NEB). Kits were used according to
405 manufacturer's instructions.
406
407 Cell culture and transfection of HEK-P1KO cells for electrophysiology experiments were
408 conducted as previously reported[1].
409
410
411 Electrophysiology
412 Patch-clamp experiments in transiently transfected HEK-P1KO cells were performed in standard
413 whole-cell and cell-attached mode using a Multi-clamp700A amplifier (Axon Instruments) and
414 followed the procedures described in our previous report[2].
415
416
417 Data availability
418 Cryo-EM maps of OSCA3.1 in nanodiscs has been deposited to the Electron Microscopy Data Bank
419 (EMDB) under accession number EMD-41911 with the LocalDeblur map as the primary map. The
420 corresponding atomic coordinates have been deposited to the Protein Data Bank (PDB) under ID
421 8U53.
422
423
424
425 Author contributions:
426 S.J.C. and W.H.L. cloned expression constructs and mutants. S.J.C. prepared protein samples and
427 acquired cryo-EM data. S.J.C. processed data and built and refined the atomic structures. A.E.D.
428 carried out electrophysiology experiments and analyzed data. A.B.W. supervised the project.
429 S.J.C. and A.E.D. drafted the manuscript, which was edited and finalized with contributions from
430 all authors.
431
432

Acknowledgements:

We thank W. Anderson for management the electron microscopy facility at Scripps Research, J. Torres for help with data collection, and C. Bowman, L. Dong and J.C. Ducom for assistance with computation. We acknowledge members of the Ward laboratory. This work was supported by NIH grant R01 HL143297 and a Ray Thomas Edwards Foundation grant to A.B.W. A.E.D was supported by grant R35 NS105067.

Molecular graphics and analyses performed with UCSF Chimera and UCSF ChimeraX, developed by the Resource for Biocomputing, Visualization, and Informatics at the University of California, San Francisco, with support from National Institutes of Health R01-GM129325 and P41-GM103311, and the Office of Cyber Infrastructure and Computational Biology, National Institute of Allergy and Infectious Diseases.

445 **References**

446 1 Jojoa-Cruz, S. *et al.* Cryo-EM structure of the mechanically activated ion channel OSCA1.2.
447 *Elife* **7** (2018). https://doi.org:10.7554/eLife.41845
448 2 Murthy, S. E. *et al.* OSCA/TMEM63 are an Evolutionarily Conserved Family of Mechanically
449 Activated Ion Channels. *Elife* **7** (2018). https://doi.org:10.7554/eLife.41844
450 3 Ranade, S. S., Syeda, R. & Patapoutian, A. Mechanically Activated Ion Channels. *Neuron*
451 **87**, 1162-1179 (2015). https://doi.org:10.1016/j.neuron.2015.08.032
452 4 Haswell, E. S., Phillips, R. & Rees, D. C. Mechanosensitive Channels: What Can They Do
453 and How Do They Do It? *Structure* **19**, 1356-1369 (2011).
454 https://doi.org:10.1016/j.str.2011.09.005
455 5 Li, Y. *et al.* Genome-wide survey and expression analysis of the OSCA gene family in rice.
456 *BMC Plant Biol* **15**, 261 (2015). https://doi.org:10.1186/s12870-015-0653-8
457 6 Zhang, M. *et al.* Structure of the mechanosensitive OSCA channels. *Nat Struct Mol Biol* **25**,
458 850-858 (2018). https://doi.org:10.1038/s41594-018-0117-6
459 7 Liu, X., Wang, J. & Sun, L. Structure of the hyperosmolality-gated calcium-permeable
460 channel OSCA1.2. *Nat Commun* **9**, 5060 (2018). https://doi.org:10.1038/s41467-018-
461 07564-5
462 8 Maity, K. *et al.* Cryo-EM structure of OSCA1.2 from Oryza sativa elucidates the mechanical
463 basis of potential membrane hyperosmolality gating. *Proc Natl Acad Sci U S A* **116**, 14309-
464 14318 (2019). https://doi.org:10.1073/pnas.1900774116
465 9 Kiyosue, T., Yamaguchi-Shinozaki, K. & Shinozaki, K. Cloning of cDNAs for genes that are
466 early-responsive to dehydration stress (ERDs) in Arabidopsis thaliana L.: identification of
467 three ERDs as HSP cognate genes. *Plant Mol Biol* **25**, 791-798 (1994).
468 https://doi.org:10.1007/BF00028874
469 10 Jojoa-Cruz, S., Burendei, B., Lee, W. H. & Ward, A. B. Structure of mechanically activated
470 ion channel OSCA2.3 reveals mobile elements in the transmembrane domain. *Structure*
471 (2023). https://doi.org:10.1016/j.str.2023.11.009
472 11 Zhang, M., Shan, Y., Cox, C. D. & Pei, D. A mechanical-coupling mechanism in
473 OSCA/TMEM63 channel mechanosensitivity. *Nat Commun* **14**, 3943 (2023).
474 https://doi.org:10.1038/s41467-023-39688-8
475 12 Drin, G. & Antonny, B. Amphipathic helices and membrane curvature. *FEBS Lett* **584**,
476 1840-1847 (2010). https://doi.org:10.1016/j.febslet.2009.10.022
477 13 Brohawn, S. G., Campbell, E. B. & MacKinnon, R. Physical mechanism for gating and
478 mechanosensitivity of the human TRAAK K+ channel. *Nature* **516**, 126-130 (2014).
479 https://doi.org:10.1038/nature14013
480 14 Bavi, N. *et al.* The role of MscL amphipathic N terminus indicates a blueprint for bilayer-
481 mediated gating of mechanosensitive channels. *Nat Commun* **7**, 11984 (2016).
482 https://doi.org:10.1038/ncomms11984
483 15 Saotome, K. *et al.* Structure of the mechanically activated ion channel Piezo1. *Nature* **554**,
484 481-486 (2018). https://doi.org:10.1038/nature25453
485 16 Paulino, C., Kalienkova, V., Lam, A. K. M., Neldner, Y. & Dutzler, R. Activation mechanism
486 of the calcium-activated chloride channel TMEM16A revealed by cryo-EM. *Nature* **552**,
487 421-425 (2017). https://doi.org:10.1038/nature24652

17 Alvadia, C. *et al.* Cryo-EM structures and functional characterization of the murine lipid scramblase TMEM16F. *Elife* **8** (2019). https://doi.org:10.7554/eLife.44365

18 Bushell, S. R. *et al.* The structural basis of lipid scrambling and inactivation in the endoplasmic reticulum scramblase TMEM16K. *Nat Commun* **10**, 3956 (2019). https://doi.org:10.1038/s41467-019-11753-1

19 Bulley, S. *et al.* TMEM16A/ANO1 channels contribute to the myogenic response in cerebral arteries. *Circ Res* **111**, 1027-1036 (2012). https://doi.org:10.1161/CIRCRESAHA.112.277145

20 Dutta, A. K., Woo, K., Khimji, A. K., Kresge, C. & Feranchak, A. P. Mechanosensitive Cl-secretion in biliary epithelium mediated through TMEM16A. *Am J Physiol Gastrointest Liver Physiol* **304**, G87-98 (2013). https://doi.org:10.1152/ajpgi.00154.2012

21 Duncan, A. L., Song, W. & Sansom, M. S. P. Lipid-Dependent Regulation of Ion Channels and G Protein-Coupled Receptors: Insights from Structures and Simulations. *Annu Rev Pharmacol Toxicol* **60**, 31-50 (2020). https://doi.org:10.1146/annurev-pharmtox-010919-023411

22 Brohawn, S. G., Su, Z. & MacKinnon, R. Mechanosensitivity is mediated directly by the lipid membrane in TRAAK and TREK1 K+ channels. *Proc Natl Acad Sci U S A* **111**, 3614-3619 (2014). https://doi.org:10.1073/pnas.1320768111

23 Kern, D. M. *et al.* Structural basis for assembly and lipid-mediated gating of LRRC8A:C volume-regulated anion channels. *Nat Struct Mol Biol* **30**, 841-852 (2023). https://doi.org:10.1038/s41594-023-00944-6

24 Pliotas, C. *et al.* The role of lipids in mechanosensation. *Nat Struct Mol Biol* **22**, 991-998 (2015). https://doi.org:10.1038/nsmb.3120

25 Zhang, Y. *et al.* Visualization of the mechanosensitive ion channel MscS under membrane tension. *Nature* **590**, 509-514 (2021). https://doi.org:10.1038/s41586-021-03196-w

26 Jojoa-Cruz, S. *et al.* Structural insights into the Venus flytrap mechanosensitive ion channel Flycatcher1. *Nat Commun* **13**, 850 (2022). https://doi.org:10.1038/s41467-022-28511-5

27 Reddy, B., Bavi, N., Lu, A., Park, Y. & Perozo, E. Molecular basis of force-from-lipids gating in the mechanosensitive channel MscS. *Elife* **8** (2019). https://doi.org:10.7554/eLife.50486

28 Brohawn, S. G., del Marmol, J. & MacKinnon, R. Crystal structure of the human K2P TRAAK, a lipid- and mechano-sensitive K+ ion channel. *Science* **335**, 436-441 (2012). https://doi.org:10.1126/science.1213808

29 Zheng, W. *et al.* TMEM63 proteins function as monomeric high-threshold mechanosensitive ion channels. *Neuron* (2023). https://doi.org:10.1016/j.neuron.2023.07.006

30 Kalienkova, V. *et al.* Stepwise activation mechanism of the scramblase nhTMEM16 revealed by cryo-EM. *Elife* **8** (2019). https://doi.org:10.7554/eLife.44364

31 Flegler, V. J. *et al.* Mechanosensitive channel gating by delipidation. *Proc Natl Acad Sci U S A* **118** (2021). https://doi.org:10.1073/pnas.2107095118

32 Rasmussen, T. *et al.* Interaction of the Mechanosensitive Channel, MscS, with the Membrane Bilayer through Lipid Intercalation into Grooves and Pockets. *J Mol Biol* **431**, 3339-3352 (2019). https://doi.org:10.1016/j.jmb.2019.05.043

532 33 Fernandez-Ballester, G., Fernandez-Carvajal, A. & Ferrer-Montiel, A. Progress in the
533 Structural Basis of thermoTRP Channel Polymodal Gating. *Int J Mol Sci* **24** (2023).
534 https://doi.org:10.3390/ijms24010743
535 34 Jordt, S. E. & Julius, D. Molecular basis for species-specific sensitivity to "hot" chili
536 peppers. *Cell* **108**, 421-430 (2002). https://doi.org:10.1016/s0092-8674(02)00637-2
537 35 Bandell, M. *et al.* High-throughput random mutagenesis screen reveals TRPM8 residues
538 specifically required for activation by menthol. *Nat Neurosci* **9**, 493-500 (2006).
539 https://doi.org:10.1038/nn1665
540 36 Verkest, C. *et al.* Intrinsically disordered intracellular domains control key features of the
541 mechanically-gated ion channel PIEZO2. *Nat Commun* **13**, 1365 (2022).
542 https://doi.org:10.1038/s41467-022-28974-6
543 37 Richardson, J., Kotevski, A. & Poole, K. From stretch to deflection: the importance of
544 context in the activation of mammalian, mechanically activated ion channels. *FEBS J*
545 (2021). https://doi.org:10.1111/febs.16041
546 38 Suloway, C. *et al.* Automated molecular microscopy: the new Leginon system. *J Struct Biol*
547 **151**, 41-60 (2005). https://doi.org:10.1016/j.jsb.2005.03.010
548 39 Zheng, S. Q. *et al.* MotionCor2: anisotropic correction of beam-induced motion for
549 improved cryo-electron microscopy. *Nat Methods* **14**, 331-332 (2017).
550 https://doi.org:10.1038/nmeth.4193
551 40 Punjani, A., Rubinstein, J. L., Fleet, D. J. & Brubaker, M. A. cryoSPARC: algorithms for rapid
552 unsupervised cryo-EM structure determination. *Nat Methods* **14**, 290-296 (2017).
553 https://doi.org:10.1038/nmeth.4169
554 41 Zhang, K. Gctf: Real-time CTF determination and correction. *J Struct Biol* **193**, 1-12 (2016).
555 https://doi.org:10.1016/j.jsb.2015.11.003
556 42 Scheres, S. H. RELION: implementation of a Bayesian approach to cryo-EM structure
557 determination. *J Struct Biol* **180**, 519-530 (2012).
558 https://doi.org:10.1016/j.jsb.2012.09.006
559 43 Zivanov, J., Nakane, T. & Scheres, S. H. W. Estimation of high-order aberrations and
560 anisotropic magnification from cryo-EM data sets in RELION-3.1. *IUCrJ* **7**, 253-267 (2020).
561 https://doi.org:10.1107/S2052252520000081
562 44 Ramlaul, K., Palmer, C. M., Nakane, T. & Aylett, C. H. S. Mitigating local over-fitting during
563 single particle reconstruction with SIDESPLITTER. *J Struct Biol* **211**, 107545 (2020).
564 https://doi.org:10.1016/j.jsb.2020.107545
565 45 Ramirez-Aportela, E. *et al.* Automatic local resolution-based sharpening of cryo-EM maps.
566 *Bioinformatics* **36**, 765-772 (2020). https://doi.org:10.1093/bioinformatics/btz671
567 46 Vilas, J. L. *et al.* MonoRes: Automatic and Accurate Estimation of Local Resolution for
568 Electron Microscopy Maps. *Structure* **26**, 337-344 e334 (2018).
569 https://doi.org:10.1016/j.str.2017.12.018
570 47 de la Rosa-Trevin, J. M. *et al.* Xmipp 3.0: an improved software suite for image processing
571 in electron microscopy. *J Struct Biol* **184**, 321-328 (2013).
572 https://doi.org:10.1016/j.jsb.2013.09.015
573 48 de la Rosa-Trevin, J. M. *et al.* Scipion: A software framework toward integration,
574 reproducibility and validation in 3D electron microscopy. *J Struct Biol* **195**, 93-99 (2016).
575 https://doi.org:10.1016/j.jsb.2016.04.010

576 49 Sanchez-Garcia, R. *et al.* DeepEMhancer: a deep learning solution for cryo-EM volume
577 post-processing. *Commun Biol* **4**, 874 (2021). https://doi.org:10.1038/s42003-021-02399-
578 1
579 50 Waterhouse, A. *et al.* SWISS-MODEL: homology modelling of protein structures and
580 complexes. *Nucleic Acids Res* **46**, W296-W303 (2018).
581 https://doi.org:10.1093/nar/gky427
582 51 Emsley, P. & Cowtan, K. Coot: model-building tools for molecular graphics. *Acta*
583 *Crystallogr D* **60**, 2126-2132 (2004). https://doi.org:10.1107/S0907444904019158
584 52 Casanal, A., Lohkamp, B. & Emsley, P. Current developments in Coot for macromolecular
585 model building of Electron Cryo-microscopy and Crystallographic Data. *Protein Sci* **29**,
586 1069-1078 (2020). https://doi.org:10.1002/pro.3791
587 53 Liebschner, D. *et al.* Macromolecular structure determination using X-rays, neutrons and
588 electrons: recent developments in Phenix. *Acta Crystallogr D Struct Biol* **75**, 861-877
589 (2019). https://doi.org:10.1107/S2059798319011471
590 54 Afonine, P. V. *et al.* Real-space refinement in PHENIX for cryo-EM and crystallography.
591 *Acta Crystallogr D Struct Biol* **74**, 531-544 (2018).
592 https://doi.org:10.1107/S2059798318006551
593 55 Wang, R. Y. R. *et al.* Automated structure refinement of macromolecular assemblies from
594 cryo-EM maps using Rosetta. *Elife* **5** (2016). https://doi.org:ARTN e17219
595 10.7554/eLife.17219
596 56 Moriarty, N. W., Grosse-Kunstleve, R. W. & Adams, P. D. electronic Ligand Builder and
597 Optimization Workbench (eLBOW): a tool for ligand coordinate and restraint generation.
598 *Acta Crystallogr D Biol Crystallogr* **65**, 1074-1080 (2009).
599 https://doi.org:10.1107/S0907444909029436
600 57 Williams, C. J. *et al.* MolProbity: More and better reference data for improved all-atom
601 structure validation. *Protein Sci* **27**, 293-315 (2018). https://doi.org:10.1002/pro.3330
602 58 Barad, B. A. *et al.* EMRinger: side chain-directed model and map validation for 3D cryo-
603 electron microscopy. *Nat Methods* **12**, 943-946 (2015).
604 https://doi.org:10.1038/nmeth.3541
605 59 Afonine, P. V. *et al.* New tools for the analysis and validation of cryo-EM maps and atomic
606 models. *Acta Crystallogr D Struct Biol* **74**, 814-840 (2018).
607 https://doi.org:10.1107/S2059798318009324
608 60 Rao, S., Klesse, G., Stansfeld, P. J., Tucker, S. J. & Sansom, M. S. P. A heuristic derived from
609 analysis of the ion channel structural proteome permits the rapid identification of
610 hydrophobic gates. *Proc Natl Acad Sci U S A* **116**, 13989-13995 (2019).
611 https://doi.org:10.1073/pnas.1902702116
612 61 Klesse, G., Rao, S., Sansom, M. S. P. & Tucker, S. J. CHAP: A Versatile Tool for the Structural
613 and Functional Annotation of Ion Channel Pores. *J Mol Biol* **431**, 3353-3365 (2019).
614 https://doi.org:10.1016/j.jmb.2019.06.003
615 62 Schrödinger, L. The PyMOL Molecular Graphics System, Version 2.1 Schrödinger, LLC.
616 63 Pettersen, E. F. *et al.* UCSF Chimera--a visualization system for exploratory research and
617 analysis. *J Comput Chem* **25**, 1605-1612 (2004). https://doi.org:10.1002/jcc.20084
618 64 Goddard, T. D. *et al.* UCSF ChimeraX: Meeting modern challenges in visualization and
619 analysis. *Protein Sci* **27**, 14-25 (2018). https://doi.org:10.1002/pro.3235

620 65 Sievers, F. *et al.* Fast, scalable generation of high-quality protein multiple sequence
621 alignments using Clustal Omega. *Mol Syst Biol* **7**, 539 (2011).
622 https://doi.org:10.1038/msb.2011.75
623 66 Robert, X. & Gouet, P. Deciphering key features in protein structures with the new
624 ENDscript server. *Nucleic Acids Res* **42**, W320-324 (2014).
625 https://doi.org:10.1093/nar/gku316
626

Figures

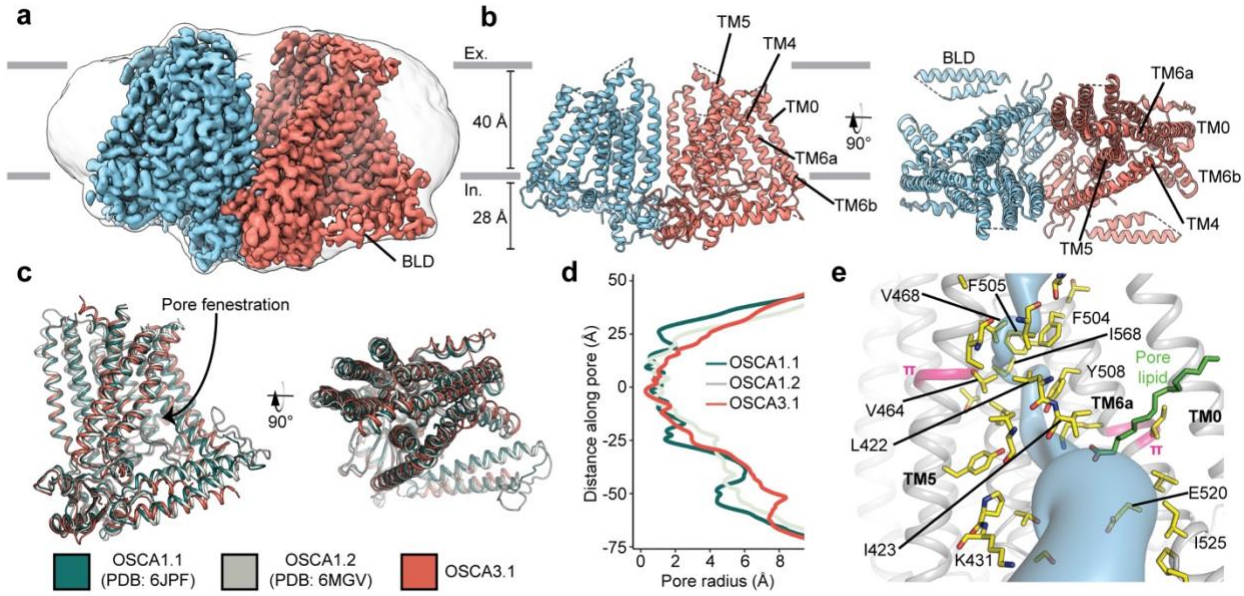

Figure 1: Cryo-EM structure and pore of OSCA3.1.
a, Cryo-EM map of OSCA3.1 dimer colored by subunit. Nanodisc density in grey corresponds to the unsharpened map (gaussian-filtered to 1.5 σ). **b,** Front (left) and top (right) view of atomic model. Ex.: Extracellular, In.: Intracellular. **c,** Superposition of OSCA1.1, OSCA1.2 (in nanodiscs) and OSCA3.1 protomers. **d,** Pore profile of OSCAs in **c**. **e,** View of the pore pathway (blue) of OSCA3.1. Pore facing residues colored in yellow, with selected residues labeled. π-helical turns in pink. Putative pore lipid in green. Backbone of TM3 and TM4 helices hidden for clarity.

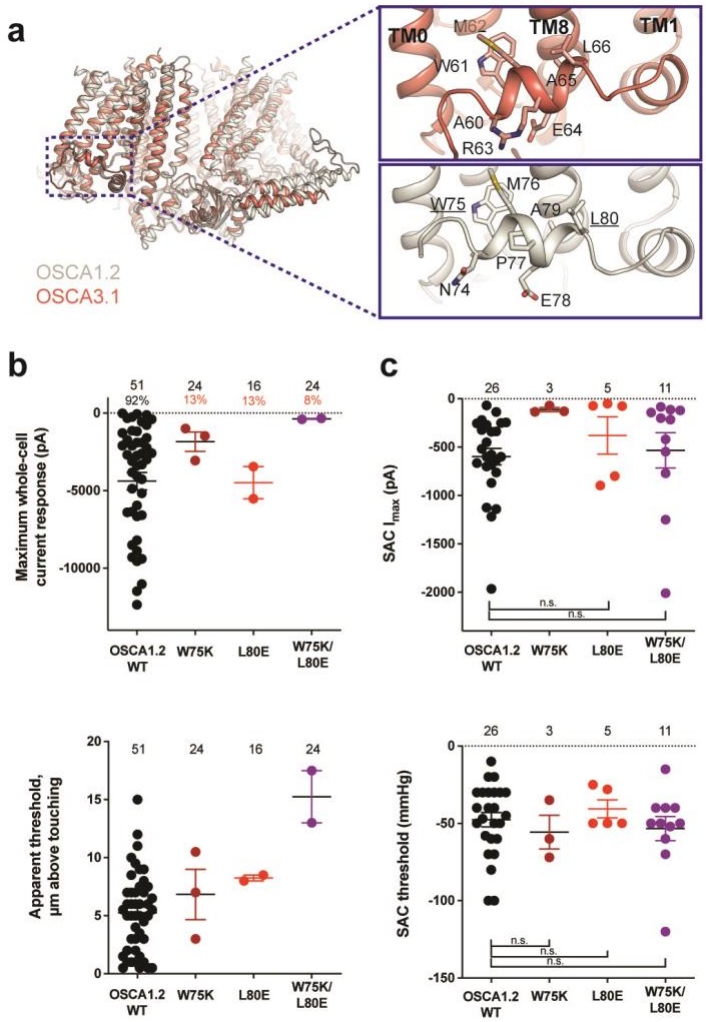

Figure 2: Amphipathic helix mutants of OSCA1.2.
a, Superposition of OSCA1.2 (grey) and OSCA3.1 (red). Insets: close-up view of amphipathic helix. Residues substituted in OSCA1.2 for electrophysiology experiments are underlined. **b,** Few cells expressing mutations in the amphipathic helix respond to poking compared to WT controls. Top panel: Maximum poke-induced currents observed in whole-cell mode for cells exposed to displacements up to 8.9 ± 0.6 µm (N=51; mean ± S.E.M.), 12.8 ± 0.7 µm (N=24), 12.4 ± 0.7 µm (N=16), and 12.8 ± 0.5 µm (N=24) above touching for WT, OSCA1.2$_{W75K}$, OSCA1.2$_{L80E}$, and OSCA1.2$_{W75K/L80E}$, respectively. Bottom panel: the apparent threshold in µm above touching the cell for this cohort. **c,** SAC maximal current (I_{max}) (top) and mmHg threshold (bottom) from WT and OSCA1.2$_{W75K/L80E}$-expressing cells reveal no significant differences in the ability of negative pressure to activate channels in cell-attached patches (Student's *t*-test). Also shown are data from single mutants OSCA1.2$_{W75K}$ and OSCA1.2$_{L80E}$. Too few patches were obtained for OSCA1.2$_{W75K}$ to compare I_{max}. Electrode resistances for **c** were similar in all cases (WT: 2.3 ± 0.1 MΩ (N=26); W75K: 2.1 ± 0.4 MΩ (N=3), L80E: 2.2 ± 0.1 MΩ (N=5), W75K/L80E: 1.8 ± 0.1 MΩ (N=11)). For panels **b-c**: individual cells are represented as scatter points; mean and S.E.M. are displayed.

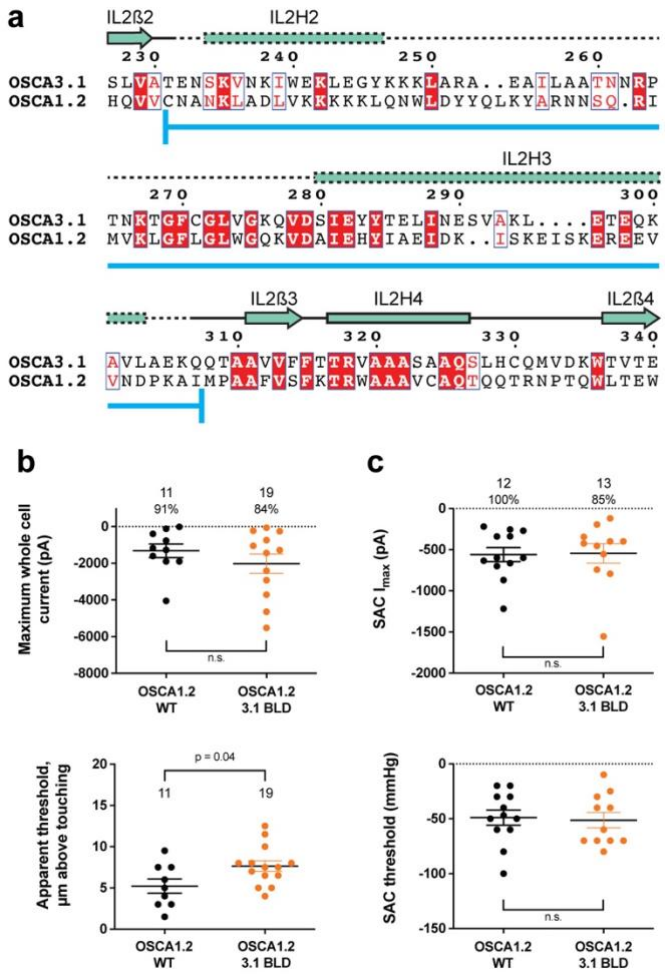

Figure 3: OSCA1.2$_{OSCA3.1\text{-}BLD}$ chimera.

a, Amino acid sequence alignment of the BLD region of OSCA1.2 and OSCA3.1. Full alignment in **Supplementary Fig. 3.** Blue line at bottom of sequences denotes the sequence swapped in OSCA1.2$_{OSCA3.1\text{-}BLD}$ chimera. **b,** Poke-induced responses are observed in HEK-P1KO cells expressing OSCA1.2$_{3.1\text{-}BLD}$. Top panel: Maximum poke-induced currents observed in whole-cell mode for cells exposed to displacements up to 9.8 ± 0.8 µm (N=11; mean ± S.E.M.) and 11.8 ± 0.6 µm (N=19) above touching for WT and OSCA1.2$_{3.1\text{-}BLD}$, respectively. The percentage of cells with responses are shown above. Bottom panel: the apparent threshold in µm above touching the cell for this cohort. **c,** SAC I_{max} (top) and mmHg threshold (bottom) from WT and OSCA1.2$_{3.1BLD}$-expressing cells reveal similar activity induced by negative pressure in cell-attached patches. Data shown were obtained from the same experiments. Electrode resistances for **c** were similar in all cases (WT: 2.4 ± 0.1 MΩ (N=12); OSCA1.2$_{OSCA3.1\text{-}BLD}$: 2.5 ± 0.1 MΩ (N=13)).

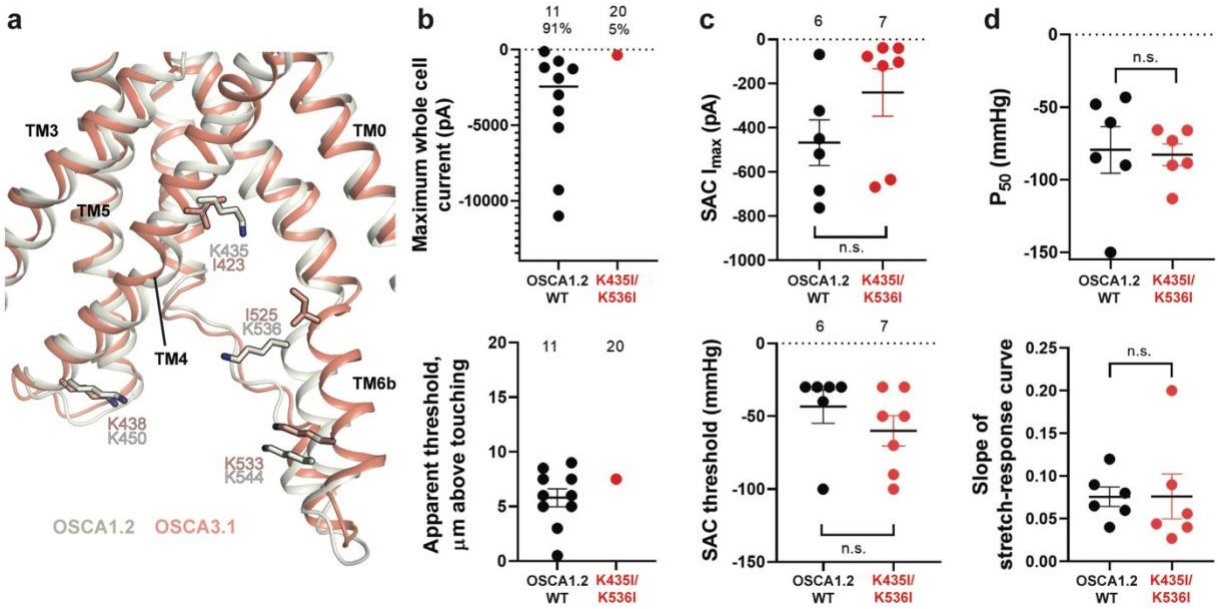

Figure 4: Probing the functional role of the potential lipid-interacting residues. **a,** Superposition of OSCA1.2 and OSCA3.1 around the pore fenestration. Residues of OSCA1.2 predicted to interact with lipids and corresponding residues in OSCA3.1 are shown. **b,** Few OSCA1.2$_{K435I/K536I}$ -expressing HEK-P1KO cells respond to the poke stimulus while nearly all cells expressing OSCA1.2 WT channels respond (percentages shown above under the N of cells tested). Top panel: Maximum poke-induced currents observed in whole-cell mode for cells exposed to displacements up to 9.7 ± 1 µm (N=11; mean ± S.E.M.) and 12.1 ± 0.6 µm (N=20) above touching for WT and OSCA1.2$_{K435I/K536I}$, respectively. Bottom panel: the apparent threshold in µm above touching the cell for this cohort. **c,** SAC Imax (top) and mmHg threshold (bottom) from WT and OSCA1.2$_{K435I/K536I}$-expressing cells reveal no significant differences in the ability of negative pressure to activate channels in cell-attached patches (Student's *t*-test). Electrode resistances were similar in all cases (WT: 2.1 ± 0.2 MΩ (N=10); K435I/K546I: 1.7 ± 0.3 MΩ (N=7)). Data were collected within 15 min of exposure of cells to high K+ used in this assay. **d,** Analysis of stimulus-response relationships reveal no significant differences (Student's *t*-test) in pressure to half-maximal activation (P_{50}; top) or the slope of the curve (bottom). Whole cell and SAC data were obtained from cells transfected at the same time.